

See discussions, stats, and author profiles for this publication at: <https://www.researchgate.net/publication/51525176>

# Synthesis and Characterization of Large-Area Graphene and Graphite Films on Commercial Cu–Ni Alloy Foils

ARTICLE *in* NANO LETTERS · AUGUST 2011

Impact Factor: 13.59 · DOI: 10.1021/nl201699j · Source: PubMed

CITATIONS

124

READS

112

8 AUTHORS, INCLUDING:



**Shanshan Chen**

Xiamen University

38 PUBLICATIONS 1,810 CITATIONS

SEE PROFILE



**Yaping Wu**

Xiamen University

26 PUBLICATIONS 806 CITATIONS

SEE PROFILE



**Junyong Kang**

Xiamen University

222 PUBLICATIONS 1,947 CITATIONS

SEE PROFILE



**Rodney Ruoff**

Ulsan National Institute of Science and Tech...

575 PUBLICATIONS 73,828 CITATIONS

SEE PROFILE

# Synthesis and Characterization of Large-Area Graphene and Graphite Films on Commercial Cu–Ni Alloy Foils

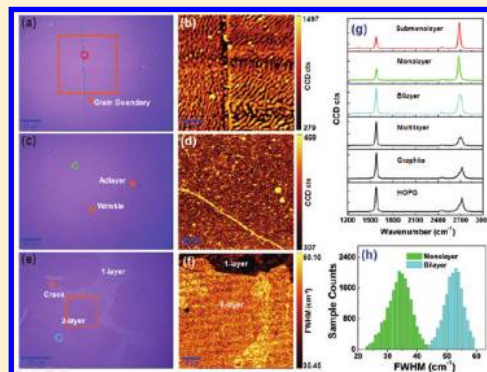
Shanshan Chen,<sup>†,‡</sup> Weiwei Cai,<sup>\*,‡</sup> Richard D. Piner,<sup>†</sup> Ji Won Suk,<sup>†</sup> Yaping Wu,<sup>†,‡</sup> Yujie Ren,<sup>†</sup> Junyong Kang,<sup>‡</sup> and Rodney S. Ruoff<sup>\*,†</sup>

<sup>†</sup>Department of Mechanical Engineering and the Texas Materials Institute, The University of Texas at Austin, Austin, Texas 78712, United States

<sup>‡</sup>Department of Physics, Xiamen University, Xiamen 361005, China

**ABSTRACT:** Controlling the thickness and uniformity during growth of multilayer graphene is an important goal. Here we report the synthesis of large-area monolayer and multilayer, particularly bilayer, graphene films on Cu–Ni alloy foils by chemical vapor deposition with methane and hydrogen gas as precursors. The dependence of the initial stages of graphene growth rate on the substrate grain orientation was observed for the first time by electron backscattered diffraction and scanning electron microscopy. The thickness and quality of the graphene and graphite films obtained on such Cu–Ni alloy foils could be controlled by varying the deposition temperature and cooling rate and were studied by optical microscopy, scanning electron microscopy, atomic force microscopy, and micro-Raman imaging spectroscopy. The optical and electrical properties of the graphene and graphite films were studied as a function of thickness.

**KEYWORDS:** Graphene, Cu–Ni foil, bilayer graphene, grain orientation, film thickness



Graphene is a one-atom-thick planar sheet of  $sp^2$ -bonded carbon atoms packed in a “honeycomb” crystal lattice.<sup>1,2</sup> It was identified by John May in 1969<sup>3</sup> and extensively studied by surface scientists since then, and more recently also by the “two-dimensional electron gas physics” community, by those interested in its potential for nanoelectronics, and by those in many other disciplines as well.<sup>1,2</sup> Transport measurements have shown that graphene can have electron and hole mobility values in excess of  $200000\text{ cm}^2\text{ V}^{-1}\text{ s}^{-1}$  at room temperature.<sup>4–6</sup> The high carrier mobility and the ability to tune the electronic conduction of graphene via the field effect make graphene a promising material for electronic applications. Mechanical exfoliation of natural graphite, kish graphite, or highly oriented pyrolytic graphite (HOPG)<sup>7–9</sup> can provide single layer graphene, but the process is time-consuming and yields relatively small area samples. The annealing of SiC substrates<sup>10–12</sup> can produce monolayer (on the Si-face) or “decoupled” multilayer graphene (on the C-face). Graphene oxide platelets can be reduced by hydrazine or other reductants, to yield “reduced graphene oxide” platelets,<sup>13–15</sup> which, at least to date, show relatively low electrical conductivity, which has been attributed to structural defects formed during the oxidation and reduction processes.

Graphite film growth or graphene formation on the surface and at grain boundaries of metals, particularly transition metals, has been reported.<sup>16–22</sup> The “metallurgical model” explains graphite formation well. Since reactive carbon species are being produced, e.g., at the metal surface by decomposing hydrocarbon gas, a concentration gradient results causing carbon atoms to diffuse into the metal, normal to the surface. The solubility of

carbon in a metal, if nonzero, increases with temperature. For example, pure nickel dissolves  $\sim 1.3$  atom % of carbon at  $1000\text{ }^\circ\text{C}$ .<sup>22</sup> Some (or based on cooling rate and metal sample geometry, essentially all) of the carbon atoms dissolved in a metal at high temperature can precipitate as a graphite film upon cooling, for relatively thin pieces of metal.<sup>22</sup> In recent work, thin Ni films and fast-cooling processes have been used to suppress the amount of precipitated carbon.<sup>23–25</sup> However, these methods yield nonuniform graphene films in a wide thickness range from 1 to  $\sim 12$  graphene layers, with monolayer regions up to  $20\text{ }\mu\text{m}$  in lateral size, which was affected by the relatively small grain size of Ni film.<sup>23</sup> Especially, Zhang et al.<sup>26</sup> observed that monolayer graphene grows inside the dimension boundaries of the metal grains while multilayer graphene ( $n \geq 3$ ) preferentially forms at the metal grain boundaries. On the other hand, due to low carbon solubility in Cu (literature values are  $<0.001$  atom % at  $1000\text{ }^\circ\text{C}$ ,<sup>27–29</sup> our recent previously published work<sup>30,31</sup> suggests it may be identically zero), large-area monolayer graphene can be synthesized on Cu by self-limiting surface deposition. Therefore, since Cu and Ni are well-known binary isomorphous systems, Cu–Ni alloy would be an ideal system which has moderate as well as controllable carbon solubility by tuning the atomic fraction of Ni in Cu.<sup>32</sup> Previously, the Cu–Ni system has been employed into synthesis of one-dimensional carbon structured materials such as carbon filaments, carbon

**Received:** January 31, 2011

**Revised:** July 25, 2011

**Published:** July 26, 2011

nanotubes, and carbon nanoclusters, due to the enhancement of the catalytic effect of Ni by alloying with Cu.<sup>33,34</sup> However, the use of a Cu–Ni alloy has rarely been studied for the two-dimensional carbon sheets—graphene growth.

A cold-wall chamber<sup>21</sup> was used to obtain monolayer, bilayer, and multilayer graphene as well as ultrathin graphite on the surfaces of Cu rich Cu–Ni alloy foils. Unlike pure Ni films or by codeposition to fabricate a Cu–Ni film, the commercial Cu–Ni foil substrates show millimeter grain size after a short time of high-temperature annealing and have moderate solubility of carbon<sup>32</sup> at temperatures around 1000 °C. They were chosen with the aim of achieving controllable thickness of multilayer graphene by precipitation during cooling and, because of their ready availability including in large area, for eventual scaling of sample size.

Polycrystalline Cu–Ni (weight percent: 31.00% Ni, 67.80% Cu, 0.45% Mn, 0.60% Fe, and 0.07% Zn, All Metal Sales, Inc.) foil with 200  $\mu\text{m}$  thickness was cut into  $10 \times 100 \text{ mm}^2$  pieces and loaded into a homemade cold-wall reactor.<sup>21,22</sup> Before deposition, the reactor chamber was pumped to  $8 \times 10^{-2}$  Torr. Next, the substrate temperature was set to 1000 °C for 4 min under 8 Torr  $\text{H}_2$  (Airgas, 99.999%) in order to remove the metal oxide as well as enlarge the substrate grain size. During carbon deposition, each substrate was held for 3 min at a specific temperature (930, 975, 1000, or 1030 °C) at a pressure of 8 Torr of methane gas (Airgas, 99.999%). In the carbon deposition step, methane decomposes on the substrate surface freeing carbon atoms which then dissolve into the substrate and form a metal–C alloy within a few minutes. After deposition, each substrate was cooled down with a cooling rate either of 100 °C/s or of 5 °C/s, and it is during cooling that either graphene or graphite precipitates on the substrate surface. Our experiments generated seven samples labeled S-930-100, S-975-100, S-1000-100, S-1030-100, S-975-5, S-1000-5, and S-1030-5. The capital S stands for sample, the first number as read from left to right indicates the temperature in °C that the sample was held at for 3 min during exposure to methane and hydrogen, and the last number represents the cooling rate in °C/s that the sample was cooled down at, after the 3-min duration high temperature exposure to methane.

After etching the metal substrate from the samples in an aqueous  $\text{Fe}(\text{NO}_3)_3$  solution (1 M),<sup>30,35,36</sup> each film was transferred to either a glass slide, a  $\text{SiO}_2/\text{Si}$  wafer, or one of various other substrates. During this process the graphene on the Cu–Ni foil sample was spin-coated with a thin layer of poly(methyl methacrylate) (PMMA), and then was floated on the etchant solution. In order to increase the etching rate, the bottom side of each foil piece was polished by sandpaper to remove the surface carbon film. Overnight exposure to the metal etchant generated a film suspended on the solution surface due to surface tension. Glass slides and wafer pieces of 285 nm thick  $\text{SiO}_2/\text{Si}$  were used to capture the floating films which were then dried in air. After transfer, graphene on glass slides or  $\text{SiO}_2/\text{Si}$  wafer pieces was obtained by removing the PMMA using acetone.

Scanning electron microscopy (SEM) images of the samples were taken with an FEI Quanta-600 FEG Environmental SEM using a voltage of 30 kV. Electron backscattered diffraction (EBSD) measurements (EDAX Pegasus integrated EDS&EBSD system) were made with a Zeiss Neon40 FE-SEM. The accelerating voltage of the primary electron beam for the backscatter images was 15 kV, and the aperture diameter was 120  $\mu\text{m}$ . A 532 nm excitation laser ( $\sim 6 \text{ mW}$ ) was used for Raman spectroscopy (WITec Alpha 300 micro-Raman imaging system).

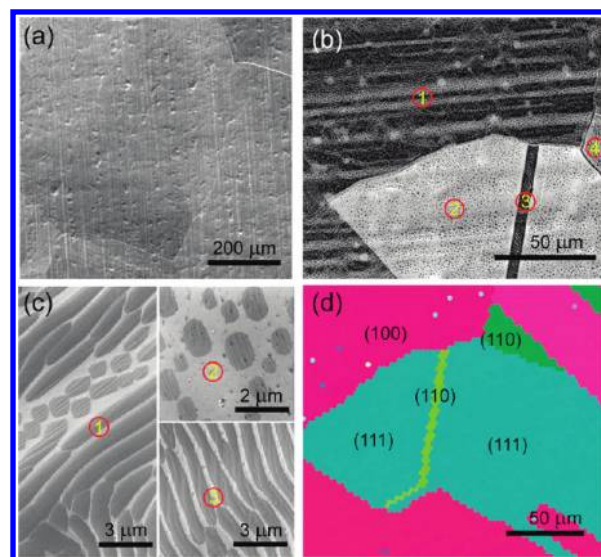
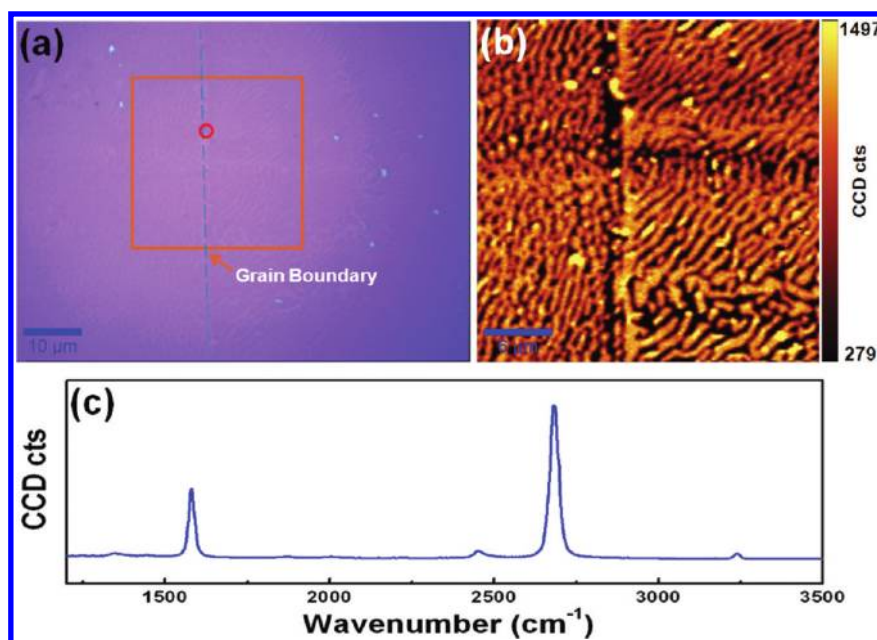


**Figure 1.** SEM images of (a) the Cu–Ni foil after annealing for 4 min at 1000 °C, and of sample S-930-100 in (b) low magnification and (c) high magnification corresponding to regions of 1–3 in (b). (d) EBSD mapping of S-930-100 taken on approximately the same area shown in (b). The deformation of the image is from a 70 °C sample tilt and long acquisition time as needed for EBSD mapping. (Discussion of regions 1–4 in (c) is in the text.)

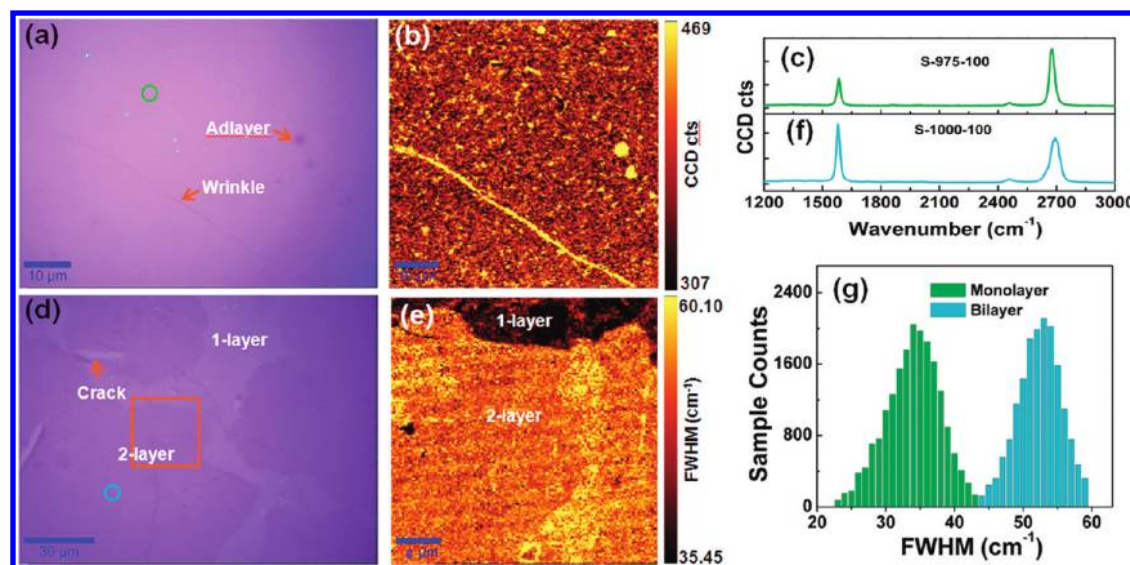
Atomic force microscopy (AFM) images were generated by a PSIA model XE-100S using noncontact mode at 300 kHz. The sheet resistance and the optical transmittance of the samples were measured by the van der Pauw four probe method (Keithley 6221 and 6514 instruments) and a spectroscopic ellipsometer system (JA Woollam M2000), respectively.

Figure 1 shows SEM images of Cu–Ni substrates with and without film deposition. The SEM image (Figure 1a) of a clean, as-annealed Cu–Ni foil at low magnification shows metal grains up to about a millimeter in size. Figure 1b shows the initial graphene growth stage from sample S-930-100. As shown in this figure, a relatively low “deposition” temperature (930 °C) causes an incomplete film to form on the substrate. The dark regions are with graphene coating while the white areas are metal oxide. When the Cu–Ni foil is removed from the reactor, the exposed metal begins to oxidize while the graphene-covered metal (the gray region) is protected from oxidation.<sup>30,37</sup> The initial graphene growth stage clearly shows different levels of coverage of graphene on different metal grains where the metal grain boundaries are clearly visible. Especially, the graphene coverage in grain 2 is much lower than that in the other grains. Higher magnification SEM images (Figure 1c) demonstrate the morphology of graphene on grains 1, 2, and 3. The graphene islands on grain 2 have a hexagonal shape elongated along the metal step. A “long stripe” structure was observed on grain 3 and there is a mixture of hexagonal and long stripes on grain 1. In order to study the dependence of graphene growth on Cu–Ni alloy grain orientation, EBSD data were acquired on the sample with submonolayer graphene (i.e., S-930-100). Figure 1d shows an EBSD mapping of approximately the same region as that of Figure 1b. Both images coincide very well despite the different sample tilt angles and the slight drift that takes place during the long acquisition time for EBSD mapping. Three grain orientations, (111), (110), and (100) were detected and mapped with EBSD. On comparison of the





**Figure 2.** Optical microscope image of S-930-100 transferred on 285 nm SiO<sub>2</sub>/Si substrate. (b) Raman mapping of the G (1530–1630 cm<sup>-1</sup>) band from the position marked by orange rectangle in (a). (c) Raman spectrum from the marked red circle in (a).



**Figure 3.** Optical and Raman images of monolayer S-975-100 (a, b) and bilayer S-1000-100 (d, e) graphene transferred onto a 285 nm SiO<sub>2</sub>/Si substrate. Raman spectra of graphene taken on the positions labeled by colored circles in (a) and (d) are shown in (c) and (f), respectively. (g) Histogram of the fwhm of Raman 2D band of monolayer and bilayer graphene.

EBSD map with the SEM image in Figure 1b, the orientation of grains 1, 2, 3, and 4 could be assigned as (100), (111), (110), and (110), respectively. The graphene film, thus, preferentially forms on the (100) surface.

To further study the growth mechanism of graphene on Cu–Ni alloy foils, sample S-930-100 was then transferred onto a 285 nm SiO<sub>2</sub>/Si substrate. Thanks to the difference of graphene morphology on different grains, we are able to distinguish the grain boundary even after transfer. As shown in Figure 2a, the color contrast under an optical microscope in the regions where there is graphene shows uniform graphene (at submonolayer coverage). The Raman spectrum (Figure 2c) recorded from the marked red

circle (Figure 2a) shows a typical feature of monolayer graphene:  $\sim 0.5 I_G/I_{2D}$  and a symmetric 2D band centered at  $\sim 2680$  cm<sup>-1</sup> with a full width at half-maximum (fwhm) of  $\sim 33$  cm<sup>-1</sup>. Moreover, the Raman G band map (a typical example is in Figure 2b) of the graphene regions has a uniform intensity both inside the grains and at the grain boundary. The observed uniformity of monolayer graphene on the Cu–Ni alloy surface is much better than the reported results on polycrystalline Ni with the monolayer graphene always interrupted by the grain boundaries by Reina<sup>23</sup> and Zhang<sup>26</sup> et al.

As the deposition temperature increases, it was then observed that when the film coverage increases as with other samples, the

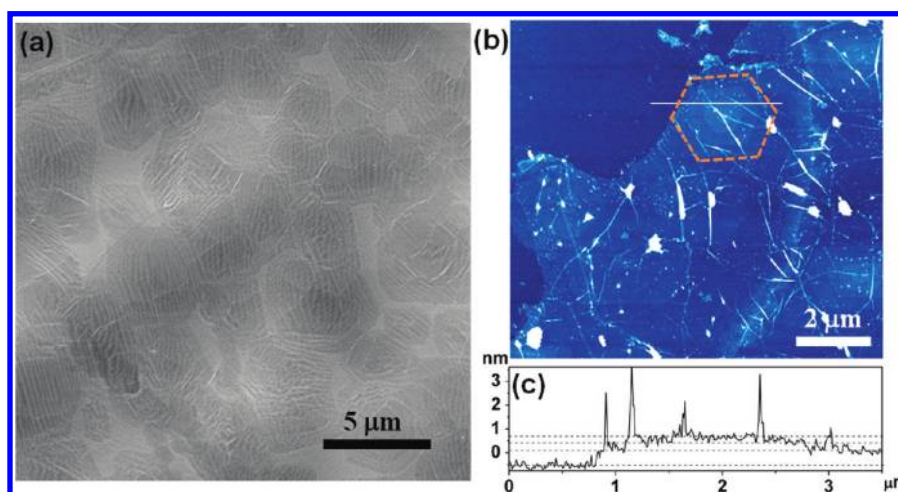


**Figure 4.** (a) SEM and (b) AFM image of S-1030-100 transferred onto a 285 nm SiO<sub>2</sub>/Si substrate. (c) Height profile was from the indicated “white” location shown in (b). The dashed lines are a guide to the eye.

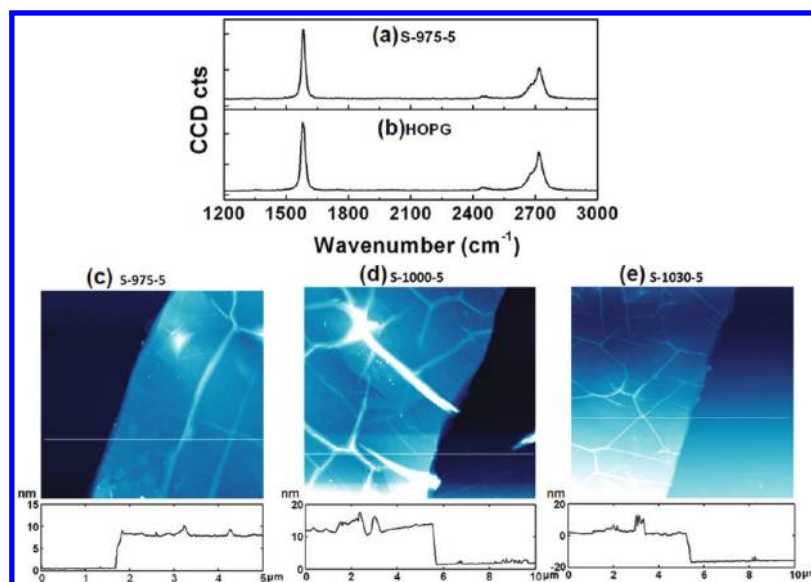


**Figure 5.** Raman spectra of sample (a) S-975-5 and (b) HOPG. (c) AFM image and height profile from the indicated white location of S-975-5, S-1000-5, and S-1030-5 transferred onto the 285 nm SiO<sub>2</sub>/Si substrates.

variation of coverage on the three different grain orientations decreases and a more uniform and continuous graphene film is obtained. Sample S-975-100 yields a uniform monolayer graphene with wrinkle and adlayers clearly observed, under an optical microscope (Figure 3a) and from Raman G band mapping (Figure 3b). The Raman spectrum (Figure 3c) from the marked green circle (Figure 3a) demonstrates the typical monolayer feature without any visible D band, indicating the high graphene quality. Sample S-1000-100 shows bilayer graphene with hundreds of micrometers in size and a coverage of around 70%, as can be seen from Figure 3d. A typical bilayer Raman spectrum (Figure 3f) from the marked blue circle in Figure 3d shows  $\sim 1 I_G/I_{2D}$  and a fwhm of 2D band of  $\sim 53 \text{ cm}^{-1}$ , suggesting the strong interlayer coupling of the bilayer graphene. Moreover, the uniformity of the Raman 2D band fwhm mapping image (Figure 3e) confirms that the bilayer

graphene grown on the Cu–Ni alloy foil was mainly AB stacked. In addition, from the histogram of the fwhm of Raman 2D band (Figure 3g), the average values of the obtained monolayer and bilayer graphene are determined to be  $34 \pm 3$  and  $53 \pm 2 \text{ cm}^{-1}$ , respectively. The highly uniform graphene thickness from samples S-975-100 and S-1000-100 might be due to the large grain size of the alloy substrate as well as the uniform carbon precipitation at grain boundaries as observed from sample S-930-100.

In order to grow multilayer graphene ( $n \geq 3$ ), the deposition temperature was then increased to  $\sim 1030^\circ\text{C}$ . Figure 4a shows the SEM image of sample S-1030-100, from where some hexagonal-shaped graphene adlayers are observed on the surface. AFM images (Figure 4b) show that such hexagonal islands are composed of stacked multilayer graphene. Compare with the uniform graphene layers obtained from lower temperature runs

(S-975-100 and S-1000-100). We suggest that such hexagonal multilayer islands are likely due to a higher methane decomposition rate<sup>38</sup> and higher carbon solubility at higher temperature, so that there is more carbon available in the Cu–Ni foil for precipitation upon cooling.

Substrates cooled down at a slower rate (5 °C/s) allowed more carbon to precipitate onto the surface and subsequently resulted in the formation of graphite films on samples S-975-5, S-1000-5, and S-1030-5. Raman spectra of these three samples exhibit the same features as HOPG (SPI-2 grade, 436HP-AB) samples routinely used in our laboratory. As an example, the Raman spectra of S-975-5 and HOPG are shown in panels a and b of Figure 5. Since Raman spectra cannot distinguish the layer number of thin graphite, AFM was performed to evaluate the thickness of the as-grown graphite films. As displayed in Figure 5c–e, the thicknesses of graphite measured from samples S-975-5, S-1000-5, and S-1030-5 are ~8, ~11, and ~19 nm, respectively. This demonstrates that as the deposition temperature increases, more carbon was dissolved into the Cu–Ni alloy and then precipitated on the surface upon cooling, and finally thicker graphite formed.

Table I summarizes the growth parameters and the thicknesses of all seven samples tested in this experiment. By optimization of the deposition temperature and the cooling rate, the thickness of the precipitated graphene and graphite films was controlled from submonolayer, monolayer, mainly bilayer, multilayer to ~19 nm ultrathin graphite. The thickness of the carbon films (i.e., number of stacked graphene layers) was not affected by the time of exposure to methane, over a range of exposure times studied. For example, at 930 °C with the cooling rate of 100 °C/s, submonolayer graphene with about the same coverage was obtained independent of the time of exposure to methane at the same pressure (8 Torr original methane pressure), or a monolayer was obtained at 975 °C and with a static charge (not dynamic pumping) of the methane, again for different exposure times and also with the same cooling rate of 100 °C/s. The thickness and morphology of graphene and graphite obtained were strongly correlated to the cooling rate. Comparing the well-known example of surface deposition of graphene on Cu versus precipitation of graphene/graphite on Ni, the graphene/graphite growth on the Cu–Ni alloy foils is also precipitation-based.

The obtained graphene and graphite films enable the study of thickness-dependent electrical and optical properties. Figure 6 shows the optical images (Figure 6a) and sheet resistance as well as transmittance values (Figure 6b,c) for films transferred onto glass slides. With increase in graphene thickness, the sheet resistance dramatically decreases with the multilayer graphene ( $n \geq 3$ ) sample having a comparable sheet resistance as that of the ~8 nm thick graphite, showing thereby a strong dependence of the electrical prosperities on multilayer graphene thickness,<sup>36</sup> more specially, as related to the interlayer coupling. On the other hand, the optical transmittance of graphene and graphite films drops at a similar slope in the observed range. A sheet resistance of 409  $\Omega/\square$  at a transmittance (at 550 nm) of 96.7% was obtained from the monolayer sample S-975-100, which is lower than that reported from Sun et al.<sup>39</sup> (at 550 nm, 1200  $\Omega/\square$ , 97.1%) but higher than a value reported by Bae et al.<sup>40</sup> (at 550 nm, 125  $\Omega/\square$ , 97.4%).

According to the Beer–Lambert law, the transmittance of light ( $T$ ) through a homogeneous material is  $T = e^{-\alpha d}$ , where  $\alpha$  is the effective absorption coefficient given by  $\alpha = 4\pi k/\lambda$ ,  $d$  is the

Table 1

sample	temperature (°C)	cooling rate (°C/s)	thickness
S-930-100	930	100	submonolayer
S-975-100	975	100	1 ML
S-1000-100	1000	100	~2 ML
S-1030-100	1030	100	2–5 ML
S-975-5	975	5	~8 nm
S-1000-5	1000	5	~11 nm
S-1030-5	1030	5	~19 nm

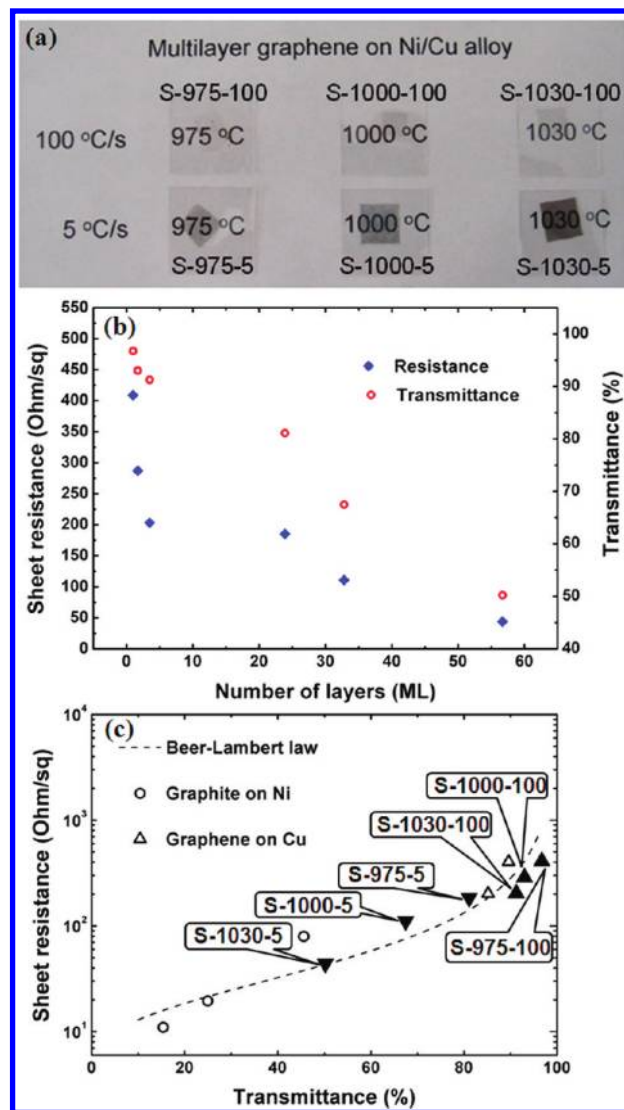


**Figure 6.** (a) Optical images of graphene and graphite films transferred on glass slides. (b) Plots of sheet resistance and transmittance (at 550 nm) as a function of graphene or graphite thickness. (c) Plots of sheet resistance as a function of transmittance, in comparison with other results:  $\circ$ , graphite films grown on Ni foils (see ref 41);  $\Delta$ , graphene grown on Cu foils (see ref 41).

film thickness,  $k$  is the extinction coefficient, and  $\lambda$  is the wavelength of the incident light. The sheet resistance is defined as  $R = 1/Gd$ , where  $G$  is the material conductivity. Combining



these equations yields<sup>41</sup>

$$R = -\frac{4\pi k}{G\lambda \ln T} \quad (1)$$

where  $k$  is 1.3.<sup>42</sup> As shown in Figure 6c, by fitting the experimental results for the ultrathin graphite samples from this work and also to results we obtained previously for growth on Ni and Cu foils,<sup>41</sup> using eq 1, the extracted  $G$  value is  $1.1 \times 10^6$  S/m. This value is slightly lower than the  $2.1 \times 10^6$  S/m for HOPG in the  $a$ – $b$  plane,<sup>43</sup> which is perhaps due to the polycrystalline property of the as-grown graphite. The sheet resistance values as a function of transmittance of graphene obtained from this work are plotted in Figure 6c as well. It is worth noting that the data points obtained from graphene are lower than the fitting curve, which indicates that graphene grown on the Cu–Ni alloy foil has higher conductance than graphite. Moreover, the data points obtained from graphite from the Cu–Ni alloy foil fill a gap between the results obtained from that of pure Ni and pure Cu foils.

This Letter presents the chemical vapor deposition synthesis and characterization of large-area graphene, primarily bilayer graphene, and graphite on Cu–Ni foils by the use of a cold-wall reactor with methane and hydrogen as precursors. The dependence of early stage island growth rate on grain orientation in the Cu–Ni foil was clearly observed for the first time. The thickness of the precipitated graphene and graphite films, which ranged from incomplete monolayer to bilayer to  $\sim 19$  nm, was controlled by varying both the deposition temperature and the cooling rate. After transfer to glass sides, the optical and electrical properties were studied as a function of film thickness. A sheet resistance as low as  $287 \Omega/\square$  with a transmittance of 93% was obtained for the bilayer film.

## AUTHOR INFORMATION

### Corresponding Author

\*E-mail: r.ruoff@mail.utexas.edu and wwcai@xmu.edu.cn.

## ACKNOWLEDGMENT

This work was supported by the Office of Naval Research, the National Science Foundation, and the DARPA Carbon Electronics for RF Applications Center. S. Chen, Y. Wu, Y. Ren are supported by the CSC Fellowship, the National Natural Science Foundation of China (grant nos. 60827004 and 90921002), and the “973” program (2011CB925600).

## REFERENCES

- (1) Dreyer, D. R.; Ruoff, R. S.; Bielawski, C. W. *Angew. Chem., Int. Ed.* **2010**, *49* (49), 9336–9344.
- (2) Zhu, Y.; Murali, S.; Cai, W.; Li, X.; Suk, J. W.; Potts, J. R.; Ruoff, R. S. *Adv. Mater.* **2010**, *22*, 3906–3924.
- (3) May, J. W. *Surf. Sci.* **1969**, *17* (1), 267–270.
- (4) Chen, J. H.; Jang, C.; Xiao, S. D.; Ishigami, M.; Fuhrer, M. S. *Nat. Nanotechnol.* **2008**, *3* (4), 206–209.
- (5) Morozov, S. V.; Novoselov, K. S.; Katsnelson, M. I.; Schedin, F.; Elias, D. C.; Jaszczak, J. A.; Geim, A. K. *Phys. Rev. Lett.* **2008**, *100* (1), 016602.
- (6) Zhang, Y. B.; Tan, Y. W.; Stormer, H. L.; Kim, P. *Nature* **2005**, *438* (7065), 201–204.
- (7) Lu, X. K.; Yu, M. F.; Huang, H.; Ruoff, R. S. *Nanotechnology* **1999**, *10* (3), 269–272.
- (8) Novoselov, K. S.; Geim, A. K.; Morozov, S. V.; Jiang, D.; Zhang, Y.; Dubonos, S. V.; Grigorieva, I. V.; Firsov, A. A. *Science* **2004**, *306* (5696), 666–669.

- (9) Lu, X. K.; Huang, H.; Nemchuk, N.; Ruoff, R. S. *Appl. Phys. Lett.* **1999**, *75* (193), 124316.
- (10) Ohta, T.; Bostwick, A.; Seyller, T.; Horn, K.; Rotenberg, E. *Science* **2006**, *313* (5789), 951–954.
- (11) Berger, C.; Song, Z. M.; Li, X. B.; Wu, X. S.; Brown, N.; Naud, C.; Mayou, D.; Li, T. B.; Hass, J.; Marchenkov, A. N.; Conrad, E. H.; First, P. N.; de Heer, W. A. *Science* **2006**, *312* (5777), 1191–1196.
- (12) Jernigan, G. G.; VanMil, B. L.; Tedesco, J. L.; Tischler, J. G.; Glaser, E. R.; Davidson, A.; Campbell, P. M.; Gaskill, D. K. *Nano Lett.* **2009**, *9* (7), 2605–2609.
- (13) Stankovich, S.; Dikin, D. A.; Dommett, G. H. B.; Kohlhaas, K. M.; Zimney, E. J.; Stach, E. A.; Piner, R. D.; Nguyen, S. T.; Ruoff, R. S. *Nature* **2006**, *442* (7100), 282–286.
- (14) Stankovich, S.; Dikin, D. A.; Piner, R. D.; Kohlhaas, K. A.; Kleinhammes, A.; Jia, Y.; Wu, Y.; Nguyen, S. T.; Ruoff, R. S. *Carbon* **2007**, *45* (7), 1558–1565.
- (15) Zhu, Y. W.; Stoller, M. D.; Cai, W. W.; Velamakanni, A.; Piner, R. D.; Chen, D.; Ruoff, R. S. *ACS Nano* **2010**, *4* (2), 1227–1233.
- (16) Robertson, S. D. *Nature* **1969**, *221*, 1044–1046.
- (17) Fedoseev, D. V.; Vnukov, S. P.; Derjaguin, B. V. *Carbon* **1979**, *17* (6), 453–458.
- (18) Fujita, D.; Homma, T. *Surf. Interface Anal.* **1992**, *19* (1–12), 430–434.
- (19) Obratsov, A. N.; Obratsova, E. A.; Tyurnina, A. V.; Zolotukhin, A. A. *Carbon* **2007**, *45* (10), 2017–2021.
- (20) Yu, Q. K.; Lian, J.; Siriponglert, S.; Li, H.; Chen, Y. P.; Pei, S. S. *Appl. Phys. Lett.* **2008**, *93* (11), 113103.
- (21) Cai, W. W.; Piner, R. D.; Stadermann, F. J.; Park, S.; Shaibat, M. A.; Ishii, Y.; Yang, D. X.; Velamakanni, A.; An, S. J.; Stoller, M.; An, J. H.; Chen, D. M.; Ruoff, R. S. *Science* **2008**, *321* (5897), 1815–1817.
- (22) Cai, W. W.; Piner, R. D.; Zhu, Y. W.; Li, X. S.; Tan, Z. B.; Floresca, H. C.; Yang, C. L.; Lu, L.; Kim, M. J.; Ruoff, R. S. *Nano Res.* **2009**, *2* (11), 851–856.
- (23) Reina, A.; Jia, X. T.; Ho, J.; Nezich, D.; Son, H. B.; Bulovic, V.; Dresselhaus, M. S.; Kong, J. *Nano Lett.* **2009**, *9* (1), 30–35.
- (24) Kim, K. S.; Zhao, Y.; Jang, H.; Lee, S. Y.; Kim, J. M.; Ahn, J. H.; Kim, P.; Choi, J. Y.; Hong, B. H. *Nature* **2009**, *457* (7230), 706–710.
- (25) Park, S.; An, J.; Jung, I.; Piner, R. D.; An, S. J.; Li, X.; Velamakanni, A.; Ruoff, R. S. *Nano Lett.* **2009**, *9* (4), 1593–1597.
- (26) Zhang, Y.; Gomez, L.; Ishikawa, F. N.; Madaria, A.; Ryu, K.; Wang, C. A.; Badmaev, A.; Zhou, C. W. *J. Phys. Chem. Lett.* **2010**, *1* (20), 3101–3107.
- (27) McLellan, R. B. *Scr. Metall.* **1969**, *3* (6), 389.
- (28) Mathieu, G.; Guiot, S.; Cabane, J. *Scr. Metall.* **1973**, *7* (4), 421–425.
- (29) Lopez, G. A.; Mittemeijer, E. *Scr. Mater.* **2004**, *51* (1), 1–5.
- (30) Li, X. S.; Cai, W. W.; An, J. H.; Kim, S.; Nah, J.; Yang, D. X.; Piner, R.; Velamakanni, A.; Jung, I.; Tutuc, E.; Banerjee, S. K.; Colombo, L.; Ruoff, R. S. *Science* **2009**, *324* (5932), 1312–1314.
- (31) Li, X. S.; Cai, W. W.; Colombo, L.; Ruoff, R. S. *Nano Lett.* **2009**, *9* (12), 4268–4272.
- (32) Nicholson, M. E. *Trans. Metall. Soc. AIME* **1962**, *224*, 533–535.
- (33) Chesnokov, V. V.; Zaikovskii, V. I.; Buyanov, R. A.; Molchanov, V. V.; Plyasova, L. M. *Catal. Today* **1995**, *24* (3), 265–267.
- (34) Jong, W. J.; Lai, S. H.; Hong, K. H.; Lin, H. N.; Shih, H. C. *Diamond Relat. Mater.* **2002**, *11* (3–6), 1019–1025.
- (35) Chen, S. S.; Cai, W. W.; Chen, D.; Ren, Y.; Li, X. S.; Zhu, Y. W.; Kang, J. Y.; Ruoff, R. S. *New J. Phys.* **2010**, *12*, 125011.
- (36) Li, X. S.; Zhu, Y. W.; Cai, W. W.; Borysiak, M.; Han, B. Y.; Chen, D.; Piner, R. D.; Colombo, L.; Ruoff, R. S. *Nano Lett.* **2009**, *9* (12), 4359–4363.
- (37) Chen, S. S.; Brown, L.; Levendorf, M.; Cai, W. W.; Ju, S. Y.; Edgeworth, J.; Li, X. S.; Magnuson, W. C.; Velamakanni, A.; Piner, R. R.; Kang, J. Y.; Park, J.; Ruoff, R. S. *ACS Nano* **2011**, *5* (1), 1321–1327.
- (38) Li, X. S.; Magnuson, C.; Venugopal, A.; An, J. H.; Suk, J. W.; Han, B.; Borysiak, M.; Cai, W. W.; Colombo, L.; Ruoff, R. S. *Nano Lett.* **2010**, *10* (11), 4328–4334.

- (39) Sun, Z.; Yan, Z.; Yao, J.; Beitler, E.; Zhu, Y.; Tour, J. M. *Nature* **2010**, 468 (7323), 549–552.
- (40) Bae, S.; Kim, H.; Lee, Y.; Xu, X. F.; Park, J. S.; Zheng, Y.; Balakrishnan, J.; Lei, T.; Kim, H. R.; Song, Y. I.; Kim, Y. J.; Kim, K. S.; Ozyilmaz, B.; Ahn, J. H.; Hong, B. H.; Iijima, S. *Nat. Nanotechnol.* **2010**, 5 (8), 574–578.
- (41) Cai, W. W.; Zhu, Y. W.; Li, X. S.; Piner, R. D.; Ruoff, R. S. *Appl. Phys. Lett.* **2009**, 95, 123115.
- (42) Palik, E. D. *Handbook of Optical Constants of Solids*; Academic: New York, 1991.
- (43) Soule, D. E. *Phys. Rev.* **1958**, 112, 698–707.